

Uncertainty Principle and Angular Momentum Generation in Microscopic Fission Models

G. Scamps and A. Guilleux

Université de Toulouse, CNRS/IN2P3, L2IT, Toulouse, France

D. Regnier and A. Bernard

CEA, DAM, DIF, 91297 Arpajon, France and

Université Paris-Saclay, CEA, LMCE, 91680 Bruyères-le-Châtel, France

(Dated: December 3, 2025)

The generation of angular momentum (intrinsic spin) in fission fragments has recently attracted renewed attention. While several microscopic approaches reproduce the spin distribution qualitatively using projection techniques, the physical origin of the fragments' angular momentum in density functional theory remains unclear. In this work, we investigate the mechanisms responsible for the spin distribution of fission fragments within a microscopic TDDFT framework. We compare spin distributions obtained from projection operators with those predicted by a simple expression derived from the uncertainty relation between angle and angular momentum, where angular fluctuations are estimated using a Monte Carlo sampling of nucleon positions. We find that a large portion of the spin distribution obtained from projection methods can be explained by the uncertainty principle. Our results thus show that, within microscopic approaches, the spin of fission fragments originates primarily from quantum uncertainty associated with their orientation angle with respect to the fission axis, mainly due to quadrupole deformation and, to a lesser extent, octupole deformation.

The uncertainty principle, first formulated by Heisenberg [1] and later generalized by Robertson [2], expresses a fundamental quantum limitation on the simultaneous knowledge of conjugate variables. Beyond the well-known position-momentum relation, this principle also applies to angular observables, linking the dispersion of angular momentum to that of the orientation angle. The uncertainty principle not only limits measurement precision but also fundamentally characterizes the nature of quantum states. In particular, the angle-angular momentum uncertainty relation [3] implies that a well-defined orientation of a system necessarily leads to a finite spread in its angular momentum components, typically following a spin cut-off distribution. A rare case of phenomena where that uncertainty principle play a role between spin and angle is related to the polarisation of photons [3]. In the case of fission fragments, their intrinsic deformation defines an orientation with respect to the fission axis; consequently, quantum uncertainty in this orientation naturally gives rise to a distribution of angular momenta, providing a macroscopic origin for the fragments' intrinsic spin [4–6].

The characterization of fission fragment properties is a major goal in modern studies of nuclear fission [7–9]. Among these properties, the angular momentum (or spin) of the fragments has attracted particular interest following recent experimental results [10, 11], which indicate that fragment spins exhibit a saw-tooth pattern. This pattern is often interpreted as reflecting a dependence on the deformation of the fragments. These new findings have renewed interest in both experimental [12–16] and theoretical studies.

Theoretical approaches to the generation of angular momentum in fission fragments can be broadly divided into two classes. The first consists of statistical ap-

proaches [17–21], in which fluctuations accumulate during the shape evolution from the initial configuration to scission, leading to rotational excitation of the fragments. The second consists of quantum approaches [4–6, 22–25], where quantum fluctuation, sometime related to the uncertainty principle is invoked as the source of fragment spin.

Another class of methods relies on projection techniques applied to static [26–28] or time-dependent [29–31] density-functional theory (DFT) descriptions of fission. While these microscopic approaches provide powerful tools for modeling fission, their interpretation is often less straightforward. In particular, in recent works using projection operators, the generation of angular momentum is usually discussed only in terms of a qualitative connection with fragment deformation, without addressing its fundamental origin.

In this work, we aim to clarify the source of fission fragment spin within the DFT frameworks. To this end, we use the Gogny-TDHFB code [32–37] that solve the time-dependent Hartree-Fock-Bogoliubov equation with the Gogny D1S interaction in a hybrid basis consisting of two-dimensional harmonic oscillator eigenfunctions and one-dimensional spatial mesh (the z-axis or fission axis). A mesh parameter $\Delta z = 0.8$ fm is used with $N_z = 52$ points. The oscillator wave function are restricted to $n_x + n_y \leq N_{\text{shell}}$ with $N_{\text{shell}} = 9$ and a harmonic oscillator parameter $\hbar\omega = 8$ MeV. The time propagation is solved with the Runge-Kutta method in the fourth order with a time-step $\Delta t = 2.10^{-3}$ zs.

We study three fissioning actinides, ^{230}Th , ^{240}Pu , and ^{250}Cf , which span a region of the nuclear chart where fission is asymmetric and the heavy fragment is influenced by octupole deformation [38]. These three systems also cover the range in which the characteristic saw-tooth

pattern of the fragment spin has been observed experimentally [10].

Uncertainty principle—In contrast to the well-known uncertainty relation between position and momentum, several conceptual difficulties arise in formulating an uncertainty principle between the orientation of the system and its angular momentum [3]. The first complication is that angular coordinates are periodic variables, which makes it nontrivial to define both their average values and standard deviations in a general sense. To overcome this issue, we restrict our analysis to well-oriented systems exhibiting axial symmetry around the z -axis and small fluctuations in the orientation of their principal axes. This situation occurs, for example, in nuclear fission, where the fragments are well aligned along the fission axis.

The corresponding uncertainty relation can then be written as

$$\Delta\theta \Delta L_x > \frac{1}{2}, \quad (1)$$

where L_x denotes the projection of the angular momentum along the x -direction expressed in units of \hbar and θ is the angle between the principal axis of the system and the z -axis. An analogous relation holds for L_y .

For a Gaussian wave packet in terms of θ and the azimuthal angle φ of the principal axis,

$$\Psi(\theta, \varphi) = \mathcal{N} \exp\left[-\frac{\theta^2}{4\sigma_\theta^2}\right], \quad (2)$$

the corresponding spin-cutoff distribution takes the form

$$P(L) = \frac{2L+1}{\mathcal{Z}} \exp\left[-\frac{L(L+1)}{2\sigma_L^2}\right], \quad (3)$$

where \mathcal{N} and \mathcal{Z} are normalization factors, and the widths satisfy the Heisenberg-type relation (for an intelligent state)

$$\sigma_\theta \sigma_L = \frac{1}{2}. \quad (4)$$

This simple relation illustrates that an object oriented with an angular uncertainty of about 1° corresponds to a spin cut-off distribution with an average angular momentum of approximately $29\hbar$.

The second difficulty is the composite nature of a nuclei. In collective Hamiltonian model such as [5, 6, 23] the angle wave packet is well defined. However, in microscopic model, the definition of the fluctuation of the orientation angle is much more challenging. As seen on Fig. 1, the deformed fragments are oriented along the fission axis. In general, the main orientation can be obtained by computing the principle axes of the one-body density, but is not related to an operator and so there is no trivial way of obtaining the fluctuations of that orientation.

Here we propose to estimate the distribution of the principal axis orientation going beyond the one-body

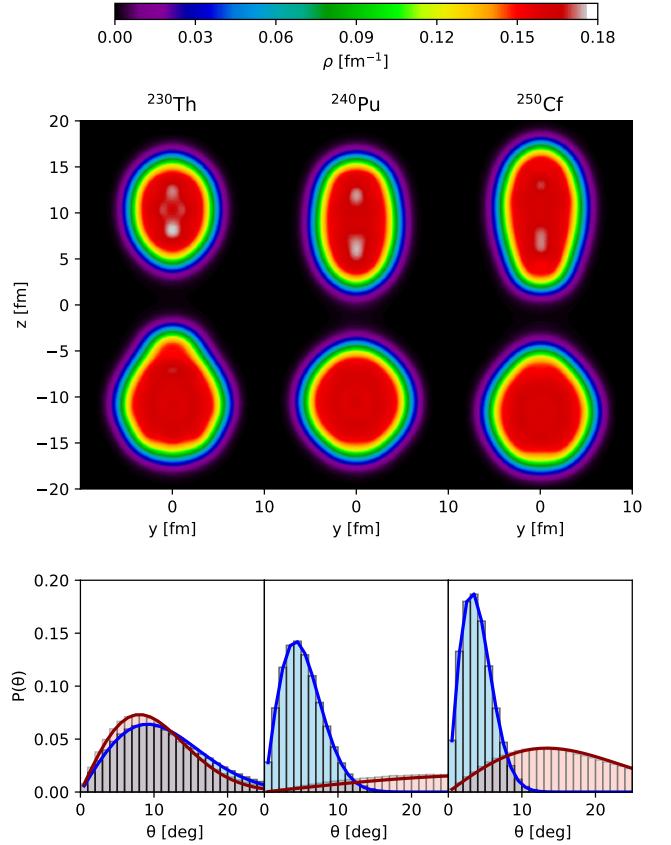


FIG. 1. Top: Slice of the density at $x = 0$ at the time when the surface of the fragments are separated by a distance of 6 fm for each fissioning system. Bottom: Corresponding angular distribution obtained by the procedure described in the text for the light fragment (blue) and heavy fragment (red). The fitted curve from eq. 5 is also shown for each fragment.

density picture. To do so, we sample the position and intrinsic spin of the neutrons and protons from the many-body density of the considered Bogoliubov vacuum projected on their good particle number. These calculations were performed with the code **NucleoScope** implementing a Markov Chain Monte Carlo algorithm to generate a representative sample of this large dimensional probability distribution [39]. For each event of this sample, we determine the principle axis of deformation of each fragment and deduce their θ angle to the z -axis (See more detail in the supplementary material). This method produces the whole distribution of probability for the θ angle from which we extract not only the expectation value θ (which is trivially 0 due to the symmetries) but also its standard deviation σ_θ .

The probability distribution of the angle θ is shown in the bottom panel of Fig. 1 for each nucleus, corresponding to the configurations displayed in the top panel. Each distribution is fitted with the function

$$f(\theta) = \mathcal{N}^2 \sin(\theta) \exp\left[-\frac{\theta^2}{2\sigma_\theta^2}\right], \quad (5)$$

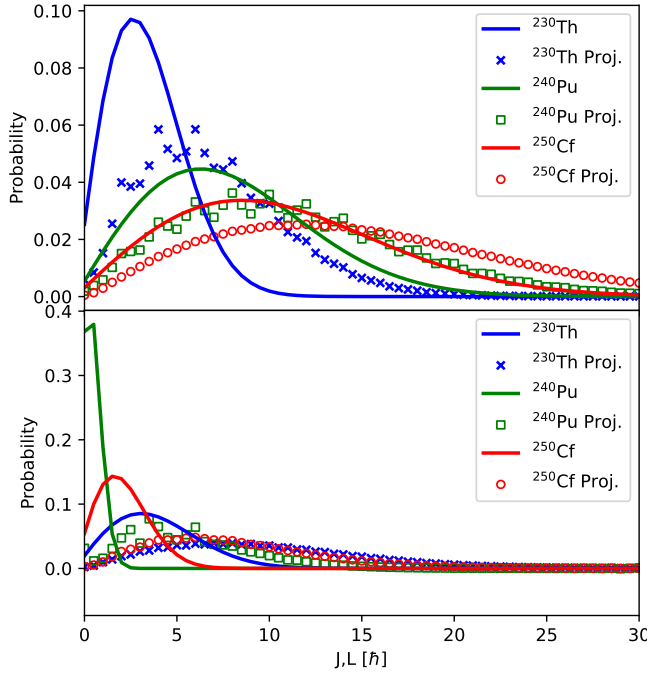


FIG. 2. Spin distribution obtained from the projection (eq. 9) compared to the spin cut-off formula (eq. 3) assuming the uncertainty principle (eq. 4) for the light (top) and heavy (bottom) fragments.

which corresponds to a Gaussian wave packet of the form given in Eq. (2). The good agreement between the calculated distributions and the fitted function indicates that the angular fluctuations are Gaussian. Moreover, the larger the quadrupole deformation of the fragment, the narrower the corresponding angular distribution becomes.

From the fluctuations of the θ angle and the uncertainty relation of Eq. (4), we can estimate spin cut-off parameters σ_L , whose values are listed in Table I. The corresponding angular momentum distributions based on Eq. 3 are shown in Fig. 2.

Nucleus	Fragment	σ_L (unc. princ.)	σ_J (overlap)	σ_J (proj)
^{230}Th	L	2.90	5.74	5.81
	H	3.37	7.84	7.88
^{240}Pu	L	6.79	9.32	9.37
	H	0.75	4.67	4.93
^{250}Cf	L	9.00	12.18	12.27
	H	2.12	6.50	6.63

TABLE I. Spin cut-off parameter for each fissioning nucleus and fragment deduced from the angle fluctuation coupled with the uncertainty principle (σ_L), from the overlap values (σ_J), and from the exact projections (σ_J).

When sampling the positions of the nucleons, it is possible to keep only events giving a specific mass split between the fragments. Computing the probability distribution of θ on such a subset of events yields the standard

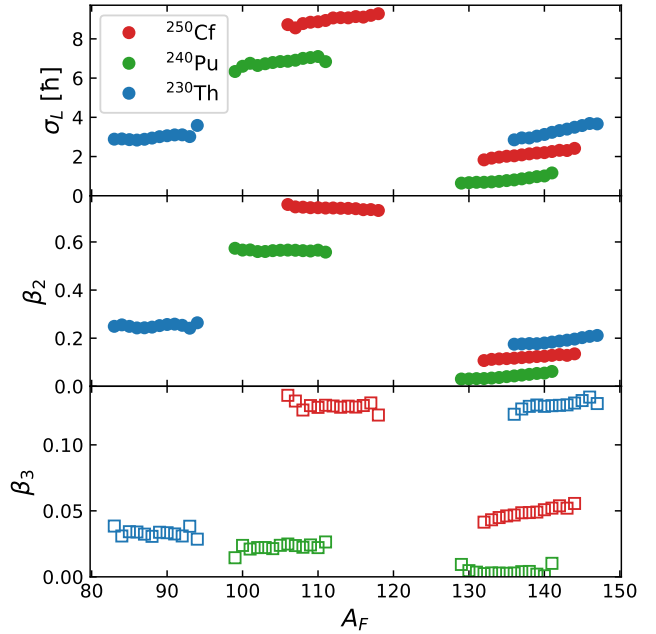


FIG. 3. Fragment-mass dependence of the angular-momentum width σ_J (top) and the quadrupole and octupole deformation parameters β_2 and $|\beta_3|$ (bottom) for the fissioning nuclei ^{230}Th , ^{240}Pu , and ^{250}Cf . Only fragments with more than 300 events are included. The angular-momentum widths σ_J are extracted from the folded angular distributions of the fragments, whereas the deformation parameters are computed from the quadrupole (solid symbols) and octupole (open symbols) moments of the fragment nucleon distributions.

deviation σ_L as a function of the mass split that we plot in the top panel of Fig. 3. The bottom panels shows the quadrupole and octupole deformation parameters, computed as

$$\beta_\lambda = \frac{4\pi}{3A(r_0 A^{1/3})^\lambda} Q_{\lambda 0}, \quad (6)$$

with $r_0 = 1.2$ fm, and

$$Q_{20} = \sqrt{\frac{5}{16\pi}} \int d^3r \rho(\mathbf{r})(2z^2 - x^2 - y^2), \quad (7)$$

$$Q_{30} = \sqrt{\frac{7}{16\pi}} \int d^3r \rho(\mathbf{r})[2z^3 - 3z(x^2 + y^2)], \quad (8)$$

where $\rho(\mathbf{r})$ is the nucleon density. This figure shows that the saw-tooth pattern of the spin distribution can be understood from the uncertainty principle: a clear correlation emerges between the quadrupole deformation parameter β_2 and the spin cut-off parameter σ_L .

Projection— The exact way of deducing the spin distribution from a HFB state $|\Psi\rangle$ is to use the projection operator [30, 40],

$$P(J_F) = \sum_{K_F} \langle \Psi | \hat{P}_{K_F K_F}^{J_F} | \Psi \rangle, \quad (9)$$

with the operator,

$$\hat{P}_{MK}^J = \frac{(2J+1)}{16\pi^2} \int d\Omega \mathcal{D}_{MK}^{J*}(\Omega) e^{i\alpha\hat{J}_z} e^{i\beta\hat{J}_y} e^{i\gamma\hat{J}_z}, \quad (10)$$

with $\Omega = (\alpha, \beta, \gamma)$ representing a separate set of the three Euler angles corresponding to a rotation of each fission fragment and $\mathcal{D}_{MK}^{J*}(\Omega)$ the Wigner D-matrix. The overlaps are determined using the Pfaffian method described in Ref. [41, 42]. To perform the rotation, the wave functions are first expanded from the hybrid basis onto a three dimensional grid with dimensions $n_x = n_y = 30$ and $n_z = 52$. The rotations are then performed exactly using the Lagrange mesh method (see more detail in the supplementary material). The resulting distribution is shown in Fig. 2 and the corresponding spin cut off parameter is listed in Table I. We see in this table that the uncertainty principle, with our method to determine the angular fluctuation, represents the dominant mechanism of angular momentum generation in well deformed fragments. We estimated, using a Monte Carlo sampler, that the fluctuation of the sum of the intrinsic spins of the nucleons is around $\sigma_s \approx 1\hbar$, which is insufficient to explain the difference between σ_L determined via the uncertainty principle and σ_J determined via the projection. We also did the same calculation with the wave-function used in Ref. [30] with similar results, showing that the present conclusion are not due to the use of the hybrid basis or the Gogny interaction.

It is remarkable that there exist also an Heisenberg-type relation with the projection, assuming a gaussian overlap

$$\langle \Psi | e^{i\alpha\hat{J}_z} e^{i\beta\hat{J}_y} e^{i\gamma\hat{J}_z} | \Psi \rangle = \exp \left[-\frac{\beta^2}{8\sigma_\beta^2} \right], \quad (11)$$

which can be deduced from a gaussian wave function eq. (2). We recover a spin cut-off distribution with a parameter σ_J corresponding to the uncertainty principle $\sigma_\beta\sigma_J = 1/2$. However, in practice the overlap after the three rotations is not gaussian because of the different K component (see Ref. [30]) create a complex dependence with α and γ . To verify the validity of the uncertainty principle, we fit the overlap $\langle \Psi | e^{i\beta\hat{J}_y} | \Psi \rangle$ with the Gaussian form of Eq. (11), and compare the deduced σ_J to the one found directly with the exact projection (see table I). we observe a very good agreement between the exact projection and the uncertainty principle computed from the overlap.

Concluding remarks— We have shown here the missing link between the deformation and the spin of the fission

sion's fragments. The more the fragments are deformed the more they are strongly oriented on the fission axis. The sampling method reveal partially this connection. However, because the principal axis of the sample only takes into account the quadrupole deformation, the deduced spin cut-off parameter underestimates the spin of the fragments. Indeed, for a fragment that get only octupole deformation and no quadrupole deformation, the principal deformation axis will show an isotropic orientation leading to a zero angular momentum. Nevertheless the octupole deformation orients the nuclei in a given direction generating additional angular momentum.

A more robust, though less intuitive, argument in favor of spin generation from the uncertainty principle in (TD)HFB arises from the relation between the Gaussian overlap and the resulting spin. As shown in Table I, the spin cut-off parameter is reproduced with better than 5% accuracy by assuming a Gaussian overlap and simply applying the uncertainty principle.

Thus, the microscopic origin of fragment spin is consistent with the macroscopic-quantal picture [4–6, 22–24]. Through a complex interplay between the structure of the fissioning nucleus, the properties of the emerging fragments, the nucleus–nucleus interaction, and the Coulomb repulsion, the fragments emerge deformed and oriented at scission. This orientation, through the uncertainty principle, gives rise to angular momentum. Additional mechanism like the breaking of pair [30] in the fragments or the coulomb excitation [6, 22, 43, 44] should also contribute to the total spin of the fragments.

Finally, although the present approach is fully dynamical, the qualitative features of the results would remain similar in static, constraint-based calculations [26–28]. In the TDDFT framework, the dynamical evolution primarily serves to excite the fragments and break nucleon pairs, thereby generating non-zero K components of the spin. The inclusion of dynamics enriches the structure of the fragment angular momentum but does not alter its fundamental origin, which remains governed by the uncertainty principle.

ACKNOWLEDGMENTS

We gratefully acknowledge support from the CNRS/IN2P3 supercomputer Center (Lyon, France) for providing computing and data-processing resources needed for this work. This work was also granted access to the HPC resources of IDRIS and CINES under Allocation No. 2024-AD010515531R1 made by GENCI.

[1] W. Heisenberg, Über den anschaulichen inhalt der quantentheoretischen kinematik und mechanik, *Zeitschrift für Physik* **43**, 172 (1927).

[2] H. P. Robertson, The uncertainty principle, *Physical Review* **34**, 163 (1929).

[3] S. Franke-Arnold, S. M. Barnett, E. Yao, J. Leach, J. Courtial, and M. Padgett, Uncertainty principle for angular position and angular momentum, *New Journal of Physics* **14**, 073019 (2012).

of Physics **6**, 103 (2004).

[4] I. Mikhailov and P. Quentin, On the spin of fission fragments, an orientation pumping mechanism, Physics Letters B **462**, 7 (1999).

[5] L. Bonneau, P. Quentin, and I. N. Mikhailov, Scission configurations and their implication in fission-fragment angular momenta, Phys. Rev. C **75**, 064313 (2007).

[6] G. Scamps and G. Bertsch, Generation, dynamics, and correlations of the fission fragments' angular momenta, Phys. Rev. C **108**, 034616 (2023).

[7] M. Bender, R. Bernard, G. Bertsch, S. Chiba, J. Dobaczewski, N. Dubray, S. A. Giuliani, K. Hagino, D. Lacroix, Z. Li, et al., Future of nuclear fission theory, Journal of Physics G: Nuclear and Particle Physics **47**, 113002 (2020).

[8] N. Schunck and D. Regnier, Theory of nuclear fission, Progress in Particle and Nuclear Physics **125**, 103963 (2022).

[9] N. Schunck and L. M. Robledo, Microscopic theory of nuclear fission: a review, Rep. Prog. Phys. **79**, 116301 (2016).

[10] J. N. Wilson *et al.*, Angular momentum generation in nuclear fission, Nature **590**, 566 (2021).

[11] M. Travar, V. Piau, A. Göök, O. Litaize, J. Nikolov, A. Oberstedt, S. Oberstedt, J. Enders, M. Peck, W. Geerts, and M. Vidali, Experimental information on mass- and TKE-dependence of the prompt fission γ -ray multiplicity, Physics Letters B **817**, 136293 (2021).

[12] S. Marin, M. S. Okar, E. P. Sansevero, I. E. Hernandez, C. A. Ballard, R. Vogt, J. Randrup, P. Talou, A. E. Lovell, I. Stetcu, O. Serot, O. Litaize, A. Chebboubi, S. D. Clarke, V. A. Protopopescu, and S. A. Pozzi, Structure in the event-by-event energy-dependent neutron- γ multiplicity correlations in $^{252}\text{Cf(sf)}$, Phys. Rev. C **104**, 024602 (2021).

[13] N. P. Giha, S. Marin, J. A. Baker, I. E. Hernandez, K. J. Kelly, M. Devlin, J. M. O'Donnell, R. Vogt, J. Randrup, P. Talou, I. Stetcu, A. E. Lovell, O. Litaize, O. Serot, A. Chebboubi, C.-Y. Wu, S. D. Clarke, and S. A. Pozzi, Correlations between energy and γ -ray emission in $^{239}\text{Pu}(n,f)$, Phys. Rev. C **107**, 014612 (2023).

[14] A. Francheteau, L. Gaudefroy, G. Scamps, O. Roig, V. Méot, A. Ebran, and G. Bélier, Scission deformation of the $^{120}\text{Cd}/^{132}\text{Sn}$ neutronless fragmentation in $^{252}\text{Cf(sf)}$, Phys. Rev. Lett. **132**, 142501 (2024).

[15] S. Marin, I. A. Tolstukhin, N. P. Giha, F. Tovesson, V. Protopopescu, and S. A. Pozzi, Measurement of fragment-correlated γ -ray emission from $^{252}\text{Cf(sf)}$, Phys. Rev. C **109**, 054617 (2024).

[16] S. Cannarozzo, S. Pomp, A. Solders, A. Al-Adili, Z. Gao, M. Lantz, H. Penttilä, A. Kankainen, I. Moore, T. Eronen, Z. Ge, J. Ruotsalainen, M. Mougeot, V. Virtanen, A. Jaries, M. Stryjczyk, and A. Raggio, Disentangling the influence of excitation energy and compound nucleus angular momentum on fission fragment angular momentum, Phys. Rev. C **111**, L031601 (2025).

[17] L. G. Moretto and R. P. Schmitt, Equilibrium statistical treatment of angular momenta associated with collective modes in fission and heavy-ion reactions, Phys. Rev. C **21**, 204 (1980).

[18] T. Døssing and J. Randrup, Dynamical evolution of angular momentum in damped nuclear reactions: (I). Accumulation of angular momentum by nucleon transfer, Nucl. Phys. A **433**, 215 (1985).

[19] J. Randrup and R. Vogt, Generation of Fragment Angular Momentum in Fission, Phys. Rev. Lett. **127**, 062502 (2021).

[20] J. Randrup, T. Døssing, and R. Vogt, Probing fission fragment angular momenta by photon measurements, Phys. Rev. C **106**, 014609 (2022).

[21] R. Vogt and J. Randrup, Angular momentum effects in fission, Phys. Rev. C **103**, 014610 (2021).

[22] G. Scamps, Microscopic description of the torque acting on fission fragments, Phys. Rev. C **106**, 054614 (2022).

[23] T. M. Shneidman, A. Rahmatinejad, G. G. Adamian, and N. V. Antonenko, Quantum-mechanical description of angular motion of fission fragments at scission, Phys. Rev. C **111**, 064621 (2025).

[24] T. M. Shneidman, G. G. Adamian, N. V. Antonenko, S. P. Ivanova, R. V. Jolos, and W. Scheid, Role of bending mode in generation of angular momentum of fission fragments, Phys. Rev. C **65**, 064302 (2002).

[25] M. Zhou, S. Chen, Z. Li, M. Smith, and Z. Li, Quantum fluctuations drive angular momenta in nuclear fission, arXiv preprint arXiv:2311.06177 (2023).

[26] G. F. Bertsch, T. Kawano, and L. M. Robledo, Angular momentum of fission fragments, Phys. Rev. C **99**, 034603 (2019).

[27] P. Marević, N. Schunck, J. Randrup, and R. Vogt, Angular momentum of fission fragments from microscopic theory, Phys. Rev. C **104**, L021601 (2021).

[28] P. Marević, N. Schunck, and M. Verriere, Microscopic theory of angular momentum distributions across the full range of fission fragments (2025), arXiv:2506.10777 [nucl-th].

[29] A. Bulgac, I. Abdurrahman, S. Jin, K. Godbey, N. Schunck, and I. Stetcu, Fission fragment intrinsic spins and their correlations, Phys. Rev. Lett. **126**, 142502 (2021).

[30] G. Scamps, I. Abdurrahman, M. Kafker, A. Bulgac, and I. Stetcu, Spatial orientation of the fission fragment intrinsic spins and their correlations, Phys. Rev. C **108**, L061602 (2023).

[31] G. Scamps, Quantal effect on the opening angle distribution between the spins of the fission fragments, Phys. Rev. C **109**, L011602 (2024).

[32] Y. Hashimoto, Linear responses in time-dependent hartree-fock-bogoliubov method with gogny interaction, The European Physical Journal A **48**, 55 (2012).

[33] Y. Hashimoto, Time-dependent hartree-fock-bogoliubov calculations using a lagrange mesh with the gogny interaction, Phys. Rev. C **88**, 034307 (2013).

[34] Y. Hashimoto and G. Scamps, Gauge angle dependence in time-dependent hartree-fock-bogoliubov calculations of $^{20}\text{O} + ^{20}\text{O}$ head-on collisions with the gogny interaction, Phys. Rev. C **94**, 014610 (2016).

[35] G. Scamps and Y. Hashimoto, Transfer probabilities for the reactions $^{14,20}\text{O} + ^{20}\text{O}$ in terms of multiple time-dependent Hartree-Fock-Bogoliubov trajectories, Phys. Rev. C **96**, 031602 (2017).

[36] G. Scamps and Y. Hashimoto, Density-constraint Time-dependent Hartree-Fock-Bogoliubov method, arXiv:1904.02945.

[37] D. Regnier, D. Lacroix, G. Scamps, and Y. Hashimoto, Microscopic description of pair transfer between two superfluid fermi systems: Combining phase-space averaging and combinatorial techniques, Physical Review C **97**, 034627 (2018).

- [38] G. Scamps and C. Simenel, Impact of pear-shaped fission fragments on mass-asymmetric fission in actinides, *Nature* **564**, 382 (2018).
- [39] A. Bernard, D. Regnier, J. Newsome, P. Carpentier, N. Dubray, and N. Pillet, Fluctuation of fission observables investigated with a monte carlo method, in preparation.
- [40] D. Zhang, D. Vretenar, T. Nikšić, P. Zhao, and J. Meng, Intrinsic spin distributions in multinucleon transfer reactions, *Physics Letters B* , 139828 (2025).
- [41] G. F. Bertsch and L. M. Robledo, Symmetry Restoration in Hartree-Fock-Bogoliubov Based Theories, *Phys. Rev. Lett.* **108**, 042505 (2012).
- [42] G. Scamps and D. Lacroix, Effect of pairing on one- and two-nucleon transfer below the coulomb barrier: A time-dependent microscopic description, *Phys. Rev. C* **87**, 014605 (2013).
- [43] J. B. Wilhelmy, E. Cheifetz, R. C. Jared, S. G. Thompson, H. R. Bowman, and J. O. Rasmussen, Angular Momentum of Primary Products Formed in the Spontaneous Fission of ^{252}Cf , *Phys. Rev. C* **5**, 2041 (1972).
- [44] J. Randrup, Effect of the coulomb force on fission fragment angular momenta, *Phys. Rev. C* **108**, 064606 (2023).

Supplemental Material : Uncertainty Principle and Angular Momentum Generation in Microscopic Fission Models

G. Scamps and A. Guilleux

Université de Toulouse, CNRS/IN2P3, L2IT, Toulouse, France

D. Regnier and A. Bernard

CEA, DAM, DIF, 91297 Arpajon, France and

Université Paris-Saclay, CEA, LMCE, 91680 Bruyères-le-Châtel, France

(Dated: December 3, 2025)

Here we provide some pertinent details to the main text.

I. CONSTRAINED HFB INITIALIZATION AND TDHFB TIME EVOLUTION

The initial configurations used for the dynamical calculations are obtained from constrained Hartree–Fock–Bogoliubov (CHFB) solutions computed with the Gogny D1S interaction. The CHFB problem is solved iteratively by direct diagonalisation in the hybrid single-particle basis. This basis consists of two-dimensional harmonic oscillator states restricted to $n_x + n_y \leq N_{\text{shell}}$ with $N_{\text{shell}} = 9$ and a one-dimensional mesh along the z axis. The number of quasiparticle states is entirely fixed by the basis size, with $N_{\text{qp}} = N_{\text{basis}} = 5720$.

To locate the asymmetric fission valley, HFB states are first generated with simultaneous quadrupole and octupole constraints. Once the system reaches the asymmetric valley, the octupole constraint is released and only the quadrupole moment is kept. This produces a sequence of configurations along the elongation coordinate. The fission path is illustrated in Fig. 1 for different values of N_{shell} .

No spatial symmetry is imposed during the CHFB or TDHFB stages. The hybrid basis allows unrestricted shapes along the fission axis. Time-reversal symmetry is broken in the TDHFB evolution.

All quasiparticle states associated with the hybrid basis are included. There is no additional quasiparticle cut-off. The evolution is performed in a finite box with fixed (Dirichlet) boundary conditions. No absorbing layer is added. The time evolution is stopped before any fragment reaches the edges of the box to avoid reflections.

Although the convergence of the potential energy surface with respect to the basis size is not fully achieved for $N_{\text{shell}} = 9$, this value represents the current computational limit of the hybrid-basis implementation with the Gogny interaction. Increasing N_{shell} would require a prohibitive number of quasiparticle states and memory resources. The present configuration already involves $N_{\text{qp}} = N_{\text{basis}} = 5720$ states and a total computational cost of about 10^4 CPU hours per fission trajectory, using MPI parallelisation. Despite this limitation, the deformation energy landscape obtained is sufficiently accurate to describe the qualitative features of the fission path and the dynamics up to scission. Increasing the number of shells would not modify the conclusions of the present

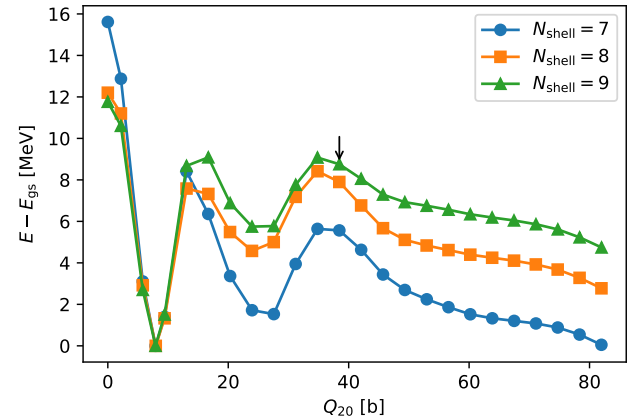


FIG. 1. Potential energy surface for ^{230}Th computed with CHFB with quadrupole and octupole constraints for different N_{shell} values. The arrow show the starting HFB state of the TDHFB calculation.

TABLE I. Properties of fragments obtained from the TDHFB calculations.

Nucleus	A_L	A_H	Z_L	Z_H	TKE [MeV]	$T_{\text{s-s}}$ [zs]
^{230}Th	87.5	142.5	35.0	55.0	153	12.3
^{240}Pu	105.3	134.7	41.9	52.1	186	6.5
^{250}Cf	112.6	137.4	44.4	53.6	178	9.6

work.

The dynamical evolution is continued until the fragments reach a separation distance of 6 fm between their skin. Once the fragments are well separated, fragment properties are extracted. These include the mass, charge, total kinetic energy, and the saddle-to-scission time. A summary of these quantities is provided in Table I for ^{230}Th , ^{240}Pu , and ^{250}Cf .

The conservation of particle number and total energy is checked throughout the TDHFB time evolution. In Fig. 2, the numerical error in both quantities remains very small during the trajectory.

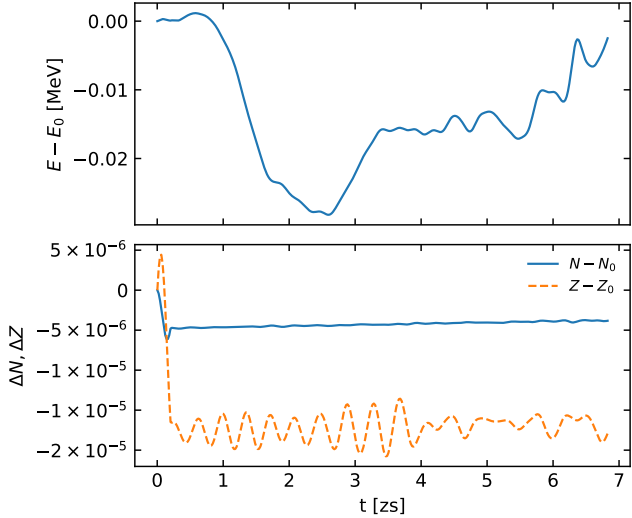


FIG. 2. Conservation of total energy (top) and particle number (bottom) during the TDHFB time evolution.

II. PREPARATION OF THE WAVE FUNCTION

Once the fragments are well separated, the TDHFB wave function in the hybrid basis is transformed to a convenient representation for further analysis. First, a Bloch–Messiah decomposition is performed on the reduced density matrices of protons and neutrons. For each isospin τ (protons or neutrons), the reduced density matrix ρ_τ is constructed from the Bogoliubov transformation matrices $V^{(\tau)}$ as

$$\rho_\tau(i, j) = \sum_k V_{ik}^{(\tau)} V_{jk}^{(\tau)*}, \quad (1)$$

and subsequently diagonalized as

$$\sum_j \rho_\tau(i, j) \varphi_\alpha^{(\tau)}(j) = n_\alpha^{(\tau)} \varphi_\alpha^{(\tau)}(i), \quad (2)$$

where $n_\alpha^{(\tau)}$ are the canonical quasiparticle occupation numbers and $\varphi_\alpha^{(\tau)}(i)$ the corresponding canonical states, expressed on the hybrid basis labeled by $i = (n_x, n_y, i_z)$.

The canonical partner of $\varphi_\alpha^{(\tau)}(i)$ is denoted by $\varphi_{\bar{\alpha}}^{(\tau)}(i)$.

The anomalous density in the canonical basis is computed as

$$\kappa_\alpha^{(\tau)} = \sum_{i,j} \varphi_\alpha^{(\tau)*}(i) \tilde{\kappa}_{ij}^{(\tau)} \varphi_{\bar{\alpha}}^{(\tau)}(j), \quad (3)$$

with

$$\tilde{\kappa}_{ij}^{(\tau)} = \sum_k V_{ik}^{(\tau)*} U_{jk}^{(\tau)}. \quad (4)$$

Due to numerical errors, the magnitude of $\kappa_\alpha^{(\tau)}$ obtained from this projection is not exactly equal to the

expected value $\sqrt{n_\alpha^{(\tau)} (1 - n_\alpha^{(\tau)})}$. A subsequent normalization is applied to enforce the correct magnitude, ensuring consistency with the canonical occupation numbers. We also enforce the properties

$$n_{\bar{\alpha}} = n_\alpha, \quad (5)$$

$$\kappa_{\bar{\alpha}} = -\kappa_\alpha, \quad (6)$$

which are also slightly broken due to the numerical errors during the time propagation.

After the Bloch–Messiah decomposition and normalization, the canonical states $\varphi_\alpha^{(\tau)}(i)$ are projected onto a three-dimensional Cartesian grid of size $n_x \times n_y \times n_z = 30 \times 30 \times 52$ with a mesh spacing of $\Delta x = 0.8$ fm.

III. NUCLEOSCOPE

A. Sampling of Many-Body Configurations

To go beyond the one-body density picture, the orientation of each fragment is extracted from many-body configurations sampled from the Bogoliubov vacuum. These configurations are generated using the NUCLEOSCOPE code, which employs a Markov Chain Monte Carlo algorithm to sample the joint probability distribution of the nucleons positions and intrinsic spins. The sampler relies on multiple independent Metropolis Markov chains characterized by a Gaussian spatial transition kernel distribution with a width 1.5 fm and a spin-flip proposal probability of 0.1. The metropolis algorithm requires estimations of ratio of probabilities for the nucleons probabilities which can be evaluated from the canonical representation of the Bogoliubov vacua following Ref. [1]. In practice, we generate a total 160×10^6 Monte Carlo events for each fissioning system out of 32 independent Markov chains. We remove from this raw sample, the first 10^5 events of each chain to account for the warm up time of the Markov chains. To mitigate the auto-correlation within each Markov chain, we finally retain only one event out of 50. We end up with a sample of more than 3×10^6 events used to actually compute observables.

For each event, the fragments are identified, and only fragment mass numbers A_F with at least 100 sampled occurrences are retained for the final θ -angle analysis as a function of A presented in the main text.

B. Determination of the Angle θ

For each event, we compute the principal deformation axis of each fragment using the quadrupole tensor

$$Q_{ij} = \sum_k (3r_{k,i}r_{k,j} - \delta_{ij}r_k^2), \quad (7)$$

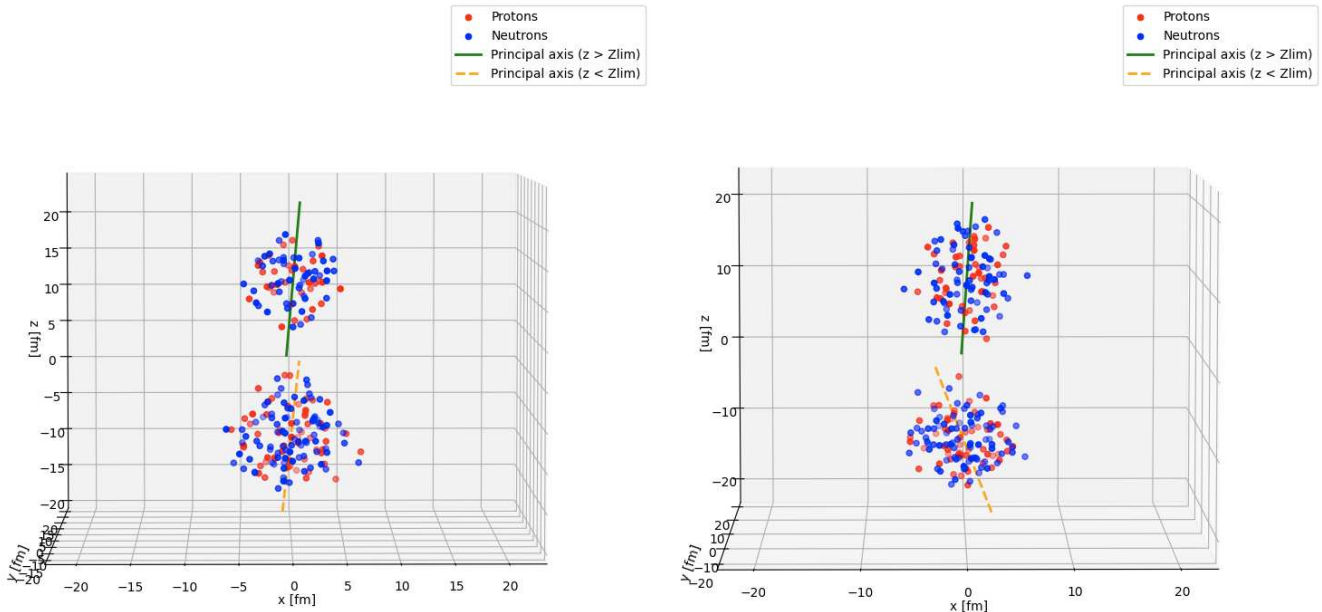


FIG. 3. Example of the determination of the principal deformation axes for two fissioning systems. The left panel corresponds to ^{230}Th , and the right panel to ^{250}Cf . The red and blue dots represent the proton and neutron spatial distributions, respectively. The green and orange lines indicate the principal axes of the fragments located above ($z > Z_{\text{lim}}$) and below ($z < Z_{\text{lim}}$) the separation plane. The angle θ is then computed as the angle between each fragment's principal symmetry axis and the global z -axis of the fission coordinate system.

where \vec{r}_k denotes the position of nucleon k relative to the fragment's center of mass. The eigenvector corresponding to the largest eigenvalue of Q_{ij} defines the principal symmetry axis of the fragment, denoted by the unit vector \hat{v} .

The orientation of this axis with respect to the fission axis (chosen as the z -axis) is characterized by the polar angle θ , defined as

$$\theta = \arccos(\hat{v} \cdot \hat{z}). \quad (8)$$

If the octupole moment Q_{30} of the fragment is negative, the axis direction is inverted ($\hat{v} \rightarrow -\hat{v}$) to ensure a consis-

tent orientation. Two examples of determination of the principal axis are shown on fig. 3. The resulting distribution of θ reflects the angular alignment of the fragment's intrinsic deformation axis relative to the fission axis.

IV. ANGULAR MOMENTUM PROJECTION

After the wave functions are prepared on a three-dimensional Cartesian grid, the projection onto angular momentum states is performed to extract the spin distributions of the fission fragments. The projection operator onto angular momentum J_F , K_F is performed by discretizing the triple integral:

$$P(J_F, K_F) = \frac{2J_F + 1}{16\pi^2} \int_0^{2\pi} d\alpha \int_0^\pi d\beta \sin \beta \int_0^{4\pi} d\gamma \mathcal{D}_{K_F K_F}^{J_F *}(\alpha, \beta, \gamma) \langle \Psi | e^{i\alpha \hat{J}_z} e^{i\beta \hat{J}_y} e^{i\gamma \hat{J}_z} | \Psi \rangle, \quad (9)$$

the α and γ integral are discretized with a uniform spacing of $\pi/8$.

The angle β is discretized using a mapping to account for the $\sin \beta$ integration weight. A uniform grid in the variable $\mu = \arccos(1 - 2\beta/\pi)$ is used, corresponding to a Gauss-Legendre quadrature in β (as in Ref. [2]), which produces denser sampling near $\beta = 0$ and $\beta = \pi$. In the present calculations, the integral over β is approximated

with $N_\beta = 32$ points.

The rotation of the wave function is performed directly in coordinate space using a cardinal sine (*sinc*) interpolation method. For each Euler angle, the spatial components of the quasiparticle wave functions are rotated around a selected axis by an angle θ . The rotation is

implemented by evaluating the transformed coordinates

$$(x', y', z') = R(\theta) (x - x_{\text{cm}}, y - y_{\text{cm}}, z - z_{\text{cm}}) + (x_{\text{cm}}, y_{\text{cm}}, z_{\text{cm}}), \quad (10)$$

and reconstructing the rotated wave function on the numerical grid using cardinal sine functions:

$$f(x', y', z') \approx \sum_{ijk} f(x_i, y_j, z_k) \text{sinc}\left(\pi \frac{x' - x_i}{\Delta x}\right) \text{sinc}\left(\pi \frac{y' - y_j}{\Delta x}\right) \text{sinc}\left(\pi \frac{z' - z_k}{\Delta x}\right), \quad (11)$$

where $\text{sinc}(x) = \sin(x)/x$. This approach preserves the spatial accuracy and continuity of the wave function inside a cutoff radius $r_{\text{cut}}=10$ fm from the fragment center of mass. Before performing the projection, the center-of-mass momentum of each fragment is removed by applying a compensating Galilean boost to the corresponding wave function, ensuring that the rotation is carried out in the fragment rest frame.

In addition to the spatial rotation, the spin components of each quasiparticle state are consistently rotated using the SU(2) spinor transformation. Each quasiparticle wave function carries a two-component spinor

$$\begin{pmatrix} \varphi_{\uparrow} \\ \varphi_{\downarrow} \end{pmatrix}, \quad (12)$$

which transforms under a rotation by an angle θ around

the axis \hat{n} as

$$\begin{pmatrix} \varphi'_{\uparrow} \\ \varphi'_{\downarrow} \end{pmatrix} = \exp\left(-\frac{i\theta}{2} \boldsymbol{\sigma} \cdot \hat{n}\right) \begin{pmatrix} \varphi_{\uparrow} \\ \varphi_{\downarrow} \end{pmatrix}, \quad (13)$$

where $\boldsymbol{\sigma}$ denotes the Pauli matrices. The combined spatial and spin rotations yield the rotated quasiparticle wave functions

$$|\Psi(\theta)\rangle = \hat{R}(\theta) |\Psi\rangle, \quad (14)$$

which are then used in the angular momentum projection integral in Eq. (9).

The overlap between the initial state and the rotated one is compute with the pfaffian method using the algorithm of Ref. [3]

- [1] M. Matsumoto and Y. Tanimura, Visualization of nuclear many-body correlations with the most probable configuration of nucleons, *Phys. Rev. C* **106**, 014307 (2022).
- [2] J. Dobaczewski, W. Satuła, B. Carlsson, J. Engel, P. Olbratowski, P. Powałowski, M. Sadziak, J. Sarich, N. Schunck, A. Staszczak, M. Stoitsov, M. Zalewski, and H. Zduńczuk, Solution of the skyrme–hartree–fock–bogolyubov equations in the cartesian deformed harmonic-oscillator basis.: (vi) hfodd (v2.40h): A new version of the program, *Computer Physics Communications* **180**, 2361 (2009).
- [3] M. Wimmer, Algorithm 923: Efficient numerical computation of the pfaffian for dense and banded skew-symmetric matrices, *ACM Trans. Math. Softw.* **38**, 30:1 (2012).